Optimizing ITER Bolometer Cameras in View of Internal Reflections and Crosstalk Between Channels

H. Meister, I. Kudashev, M. Brank, and L. C. Ingesson

Abstract— Bolometer cameras in ITER (lat.: the way) are designed as pinhole and collimator cameras, optimizing the requirements from available physical space, constraints in design options and desired line-of-sight (LOS) distribution. While for both camera types of internal reflections can be significant and lead to an increase in the effective viewing cone, collimator cameras may also suffer from crosstalk of light between channels in case internal apertures are not optimized. The concepts and simulations employed to optimize bolometer collimator cameras are presented. They are based on geometrical considerations for choosing the number and distribution of internal apertures, using the desired viewing cones as input. In the second step, ray-tracing simulations based on the Raysect packages are applied to assess internal reflections as a function of wavelength in the range IR to X-rays for the chosen geometry as well as to assess the impact of choices for material and material finishings (e.g., roughness). Examples presented focus on port-mounted bolometer cameras. The results allow us to improve the geometrical description of bolometer cameras in the ITER database of synthetic diagnostics and thus support performance assessments and studies in the preparation of tomographic reconstructions of plasma radiation. For example, the calculated measurements for LOS assuming standard radiation distributions for ITER are presented.

Index Terms— Bolometer, Cherab, ITER (lat.: the way), plasma diagnostics, ray-tracing, Raysect, synthetic diagnostic.

I. Introduction

THE total radiation emitted by the plasma and integrated over a wide spectral range is measured in many fusion devices worldwide by the bolometer diagnostic using miniaturized metal resistor bolometer sensors [1], [2]. This sensor type is also foreseen for use in ITER (lat.: the way) and will measure the plasma radiation integrated over the wavelength range from ∼1000 to ∼0.06 nm due to its 20 μm thick gold absorber. The application of up to 550 lines of sight

(LOSs) allows the reconstruction of the 2-D plasma radiation profile from line-integrated measurements using tomographic reconstruction routines [3]. The viewing cones of the LOS need to be well-defined for accurate reconstructions. For ITER, they are designed as 71 cameras of pinhole and collimator type in various sizes, which have optimized LOS distributions taking into account the requirements and constraints regarding space and environment.

ITER requires derivation of the total radiated power within 10% [4]. If one assumes that random noise accounts for half of this [5], one must ensure that all remaining sources of uncertainty and errors in the processing of bolometer measurements together contribute less than 5% (note that most sources of uncertainties and errors that remain are uncorrelated). Various sources of uncertainty and errors in the derivation of the total radiated power from bolometer measurements have been identified [5]. For example, stray radiation from the electron–cyclotron heating system can be minimized by design [6], and geometric uncertainties by design measures, metrology, and optical characterization [7], [8]. Additional sources of uncertainty and errors have been characterized, such as calibration factors (with an error of the order of 1%) [9], pressure effects [10], and correction for temperature dependence of calibration factors [11]. Compensation for other sources of uncertainty is still to be demonstrated, such as cable length and reflections on the first wall inside the vacuum vessel (in other diagnostics in the visible and UV range the reflections are a significant concern [12]). The effect of reflections inside the bolometer cameras are the topic of this article; the other sources of uncertainties and errors have been described to place the magnitude of reflections found into context.

The basic geometric parameters for ITER bolometer cameras (angle α between LOS, size P_p of front aperture and its distance L_C from sensor) have been calculated using the methods described in [13]. An example of such a typical collimator providing a high-resolution view of the divertor region of ITER is shown in Fig. 1.

Collimators made of tubes would result in significant grazing incidence reflections, which have been reduced in bolometer diagnostics by using several internal plates with apertures instead [14]. The reflection coefficient depends strongly on the angle of incidence and wavelength, as well as the material and its surface roughness, which makes estimating the impact of reflections on the bolometer measurements in a broad spectral range non-trivial. In this article, we aim to

This article has been accepted for inclusion in a future issue of this journal. Content is final as presented, with the exception of pagination.

2   IEEE TRANSACTIONS ON PLASMA SCIENCE
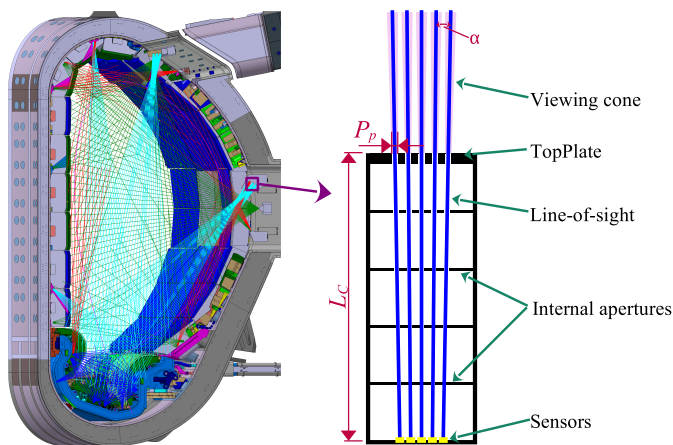

Fig. 1. Cross section of ITER with the proposed LOS distribution (left) and sketch of a collimator for a high-resolution view of the diverter region from port-mounted cameras (right). The main components of the collimator are indicated.
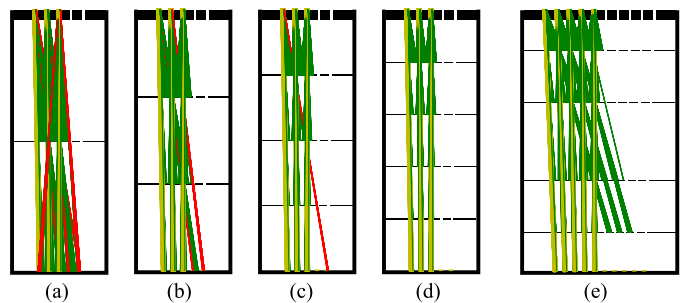

Fig. 2. (a)–(d) Optimization sequence for a collimator with five channels. Various types of rays are shown: intercepted by the camera's internal components (dark green), reaching the sensor from its allocated aperture (light green) and reaching the sensor from another aperture, that is, indicating crosstalk (red). In the case of simulated geometry four evenly spaced internal apertures fully suppress crosstalk. (e) Optimization result for a collimator with ten channels and not evenly spaced four internal apertures.

quantify any residual reflections in collimator cameras with such plates and the effectiveness of measures to reduce them.

This article presents in Section II a method to optimize the number of internal apertures given the basic geometric properties of the collimator and its viewing cones. Section III describes how Monte Carlo ray-tracing simulations have been applied to optimize collimators for ITER port-mounted cameras. The results have then been used to establish a synthetic diagnostic setup for assessing the impact of the optimization results from simulated bolometer measurements of expected plasma radiation profiles in ITER (Section IV). A conclusion of the achieved results and an outlook on further assessments required for ITER are presented in the final section.

II. CROSSTALK OF LIGHT IN COLLIMATOR CAMERAS

Collimator cameras are built such that a dedicated aperture is allocated to each sensor, in contrast to pinhole cameras, which feature one aperture that is used for all sensors within the camera. In multichannel collimator cameras, one may have to prevent light from apertures from reaching multiple sensors. Simple plates along the LOS could prevent such a crosstalk of light between channels. However, previous work has demonstrated that in such a configuration camera internal reflections significantly increase the viewing cone (in particular with pure metallic components) [7] while individual internal apertures can suppress crosstalk without such strong effects [8]. Accordingly, the design for ITER foresees metallic plates oriented perpendicularly to the main direction of the LOS (see Fig. 1). Their thickness is a compromise between providing enough structural integrity under the harsh ITER loads while offering as little surface area as possible for reflections next to the viewing cones.

To determine the minimum number of internal apertures that can suppress crosstalk of light between channels inside a collimator, a simple optimization procedure has been developed. With the locations of the sensors being defined by their placement inside ITER to achieve the desired LOS as well as the geometry of sensor prototypes [9], the relative position and size of apertures in the TopPlate (see Fig. 1) are determined

according to [13] to achieve the viewing cones such that the desired spatial resolution in the observation area is obtained while observing engineering constraints like available design space. The minimum dimensions of any internal aperture are also given by the viewing cone of the LOS. For each internal aperture, a margin may be added to its toroidal and poloidal extent to ensure that the viewing cone is determined solely by the geometry of the sensor and its allocated aperture in Top-Plate. Variations of this margin are discussed in Section III-B.

To assess if a given collimator configuration successfully suppresses crosstalk, rays of light are simulated to pass through a collimator opening toward the sensors. Along its path, it is checked if a ray intersects any internal aperture or reaches a sensor. This procedure is performed within each collimator opening such that every 0.1 mm along its poloidal dimension rays are started in the directions of the absorbers. The difference in orientation of the rays is chosen such that, based on the collimator geometry, 20 rays cover the area of a sensor (typical angular variation of $\approx 0.03°$) and the area of the left edge of the leftmost sensor up to the right edge of the right-most sensor (with reference to the sketch in Fig. 1) is covered. This is repeated for symmetry reasons only for half of the collimator openings to save computational effort.

The result of such an optimization procedure performed for the typical geometry of port-mounted collimators in ITER (collimator length $L_C = 134$ mm, angle between LOS $\alpha = 0.5°$, poloidal dimension of aperture $P_p = 7.7$ mm) is shown in Fig. 2(a)–(d). Increasing the number of internal apertures from one to four ensures that rays reaching sensors from front apertures not allocated to them (red color) are more and more intercepted by internal apertures (dark green rays) and only rays reach the sensors from those front apertures that are allocated to them (light green). In Fig. 2(e), the result of an optimization for a collimator of the same basic parameters, but with ten channels is shown. In this case, internal apertures have not been distributed evenly between sensors and TopPlate but with some extra space in the center of the collimator. This also ensures that no crosstalk occurs with the four internal apertures.

Collimators in port-mounted cameras in ITER combine ten LOSs within a structure. Using the optimization routine

This article has been accepted for inclusion in a future issue of this journal. Content is final as presented, with the exception of pagination.

MEISTER et al.: OPTIMIZING ITER BOLOMETER CAMERAS IN VIEW OF INTERNAL REFLECTIONS 3
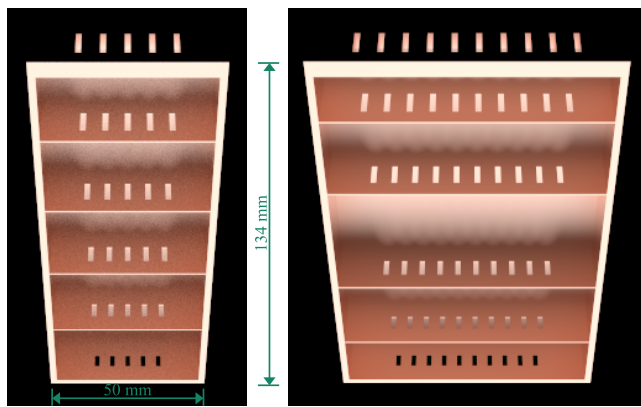

Fig. 3. Representation of the collimator geometry as used for ray-tracing for a five-channel (left) and a ten-channel (right) collimator. For visualization, the side wall has been removed, and the structure is tilted forward and illuminated from below.
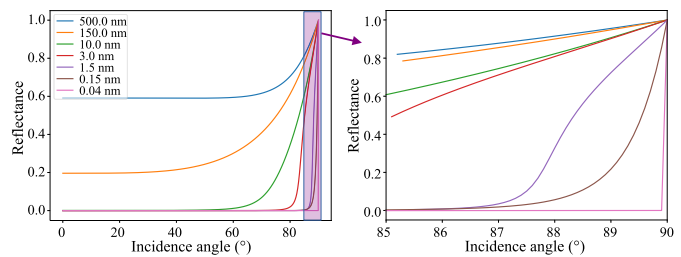

Fig. 4. Reflectance as a function of incidence angle for some chosen wavelengths for pure Cu [17], [18].

TABLE I
TOTAL POWER (W) DETECTED FOR COLLIMATOR WITH PERFECTLY ABSORBING SURFACES

2 internal apertures					
Aperture:	**1**	**2**	**3**	**4**	**5**
Sensor 1	0.0769	0	0	0.0105	0
Sensor 2	0	0.0767	0	0	0.0102
Sensor 3	0	0	0.0774	0	0
Sensor 4	0.0100	0	0	0.0776	0
Sensor 5	0	0.0103	0	0	0.0772
4 internal apertures					
Aperture:	**1**	**2**	**3**	**4**	**5**
Sensor 1	0.0774	0	0	0	0
Sensor 2	0	0.0771	0	0	0
Sensor 3	0	0	0.0771	0	0
Sensor 4	0	0	0	0.0770	0
Sensor 5	0	0	0	0	0.0772

described above, it could be shown that for all cases four internal apertures, evenly or not evenly spaced (depending on details of the viewing geometry), are sufficient to suppress crosstalk. The corresponding design parameters have been applied to the detailed design of the cameras.

III. RAY-TRACING SIMULATIONS OF REFLECTIONS

To test the impact of camera internal reflections, their dependence on wavelength, camera geometry, and surface properties, Monte Carlo ray-tracing simulations have been performed for the typical collimator geometry described above. The objective is to identify means to minimize reflections and to assess their impact on the measured signal.

A. Ray-Tracing Simulation Setup

The collimator geometry with the optimized number of internal apertures has been prepared for the ray-tracing simulations which are based on the Raysect Python library [15]. The collimator housing is built such that front and side plates with a thickness of 2 mm are placed around sensors and internal apertures. The housing is 2 cm wider than the maximum extent of apertures in the poloidal direction and toroidal direction twice the extent of the toroidal size of the apertures. Dimensions for sizes of internal aperture openings, the thickness of internal apertures, and TopPlate can be varied, and corresponding results are discussed in Section III-B. The simulated geometry of a five- and ten-channel collimator are shown in Fig. 3.

All ray-tracing simulations have been set up such that the center of the TopPlate is placed in the origin of the coordinate system oriented such that an emitter with a spectrally constant emission and intensity of 10^5 W/(m^2 sr nm) is placed above the collimator fully covering the possible field of view. Targeted pixels with $5 \cdot 10^6$ samples (i.e., number of rays generated for ray-tracing) and oriented toward the TopPlate have been placed in the locations of the sensors. As usual for the Raysect Python library, backward ray-tracing (from pixel to source) is applied. The targeted pixels as sensors accumulate all light received and integrate over the chosen wavelength range.

To assess the impact of reflections per channel, a dedicated illumination procedure has been implemented: all but one collimator opening is closed and the light power detected in every sensor is recorded. This is repeated by cycling through all collimator openings, one by one.

Special attention has been given to the materials assigned to the collimator components. As no dedicated reflection measurements for the material used for ITER cameras, CuCr1Zr (containing $\geq$98.5% Cu), are available, reflection properties of Cu have been taken and, to account for surface properties of typical machining, 25% roughening[1] has been applied. This is in line with previous measurements on samples after various machining processes and potential subsequent treatments like sandblasting [16]. The real and imaginary parts of the refractive index as measured and documented in [17] and [18] for the wavelength range of 0.025–270 μm have been imported into Raysect. The resulting reflectance with respect to the incidence angle is shown for several wavelengths in Fig. 4. In some simulations, perfectly absorbing surfaces have been used for comparison.

B. Ray-Tracing Simulation Results

As first check of the correct setup of the ray-tracing simulations, a collimator with perfectly absorbing surfaces has been analyzed and the crosstalk calculations verified. Running the simulations of five-channel collimators, once with

[1]The roughen modifier in Raysect randomly deflects the surface normal about its true position before passing the intersection parameters on to the base material. The roughness parameter takes a value in the range (0, 1] where 1 is a fully rough, lambert-like surface and 0 is a smooth, untainted surface.

This article has been accepted for inclusion in a future issue of this journal. Content is final as presented, with the exception of pagination.

4   IEEE TRANSACTIONS ON PLASMA SCIENCE
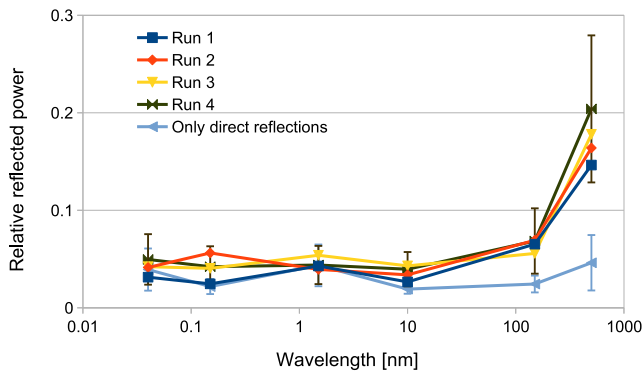

Fig. 5.   Relative reflected power over wavelength for four identical simulations with multiple reflections and one simulation considering only a single reflection.

Fig. 6.   Relative reflected power over wavelength for various values of the roughness parameter.

two and once with four internal apertures (cases b and d) in Fig. 2, respectively) yields the results shown in Table I. Comparing the ray-tracing simulation results in this table with the results shown in Fig. 2(b) and (d) demonstrates the perfect agreement regarding which sensor should receive light from which collimator opening. It also shows that the power recorded in the off-diagonal elements of the table can be used as an indication of the power of reflected light P_r that should be minimized. In the remainder of this work, only collimators optimized for completely suppressed crosstalk, that is, with the optimal number of internal apertures, will be investigated. Thus, the sum of all off-diagonal contributions will be used as a measure of detected light due to reflections. In the case of Table I for two internal apertures, this would amount to $P_r = 0.041$ W and for four internal apertures to $P_r = 0$ W.

Ray-tracing simulations have been run with several variations of the setup and for different wavelength ranges. For the latter, the ranges considered were 0.03–0.05 nm, 0.1–0.2 nm, 1–2 nm, 7–12 nm, 130–170 nm, and 400–600 nm. Comparing the relative reflected power, that is, P_r normalized to the maximum power detected at the given simulation run, shows that significant reflections are observed for wavelengths above 100 nm (see Fig. 5). The variations for the otherwise identical simulation runs 1–4 compare well to the uncertainties of individual simulation runs as provided by the Monte Carlo ray-tracing code, represented by the errorsbars that are shown for run 4. Accordingly, these uncertainties will be used in all subsequent assessments and for individual results according to Gaussian error propagation. An additional simulation considering only a single reflection (light blue curve in Fig. 5), demonstrates that the reflections for $\lambda > 100$ nm are caused by multiple reflections on the internal apertures. The latter has been confirmed by increasing the roughness parameter of the surfaces which strongly reduces the effect of multiple reflections as there is more scatter. As Fig. 6 shows, a roughness parameters of 0.1 and 0.25 are very similar within the uncertainties, a clear distinction is seen only for the reflections in the visible range. For increasing values of the roughness parameter, more and more reflections are reduced up to a value below the one for only a single reflection considered as for the latter a roughness parameter of 0.25 was used. This result is also in agreement with the reflectance of the material
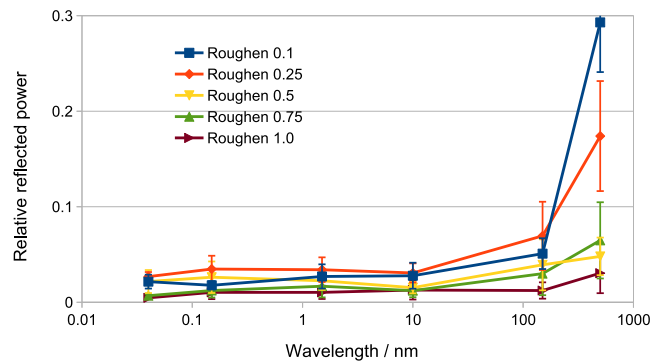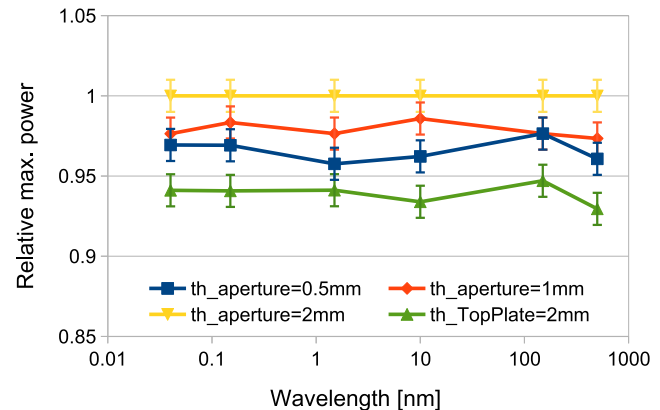

Fig. 7.   Relative maximum reflected power versus wavelength for different thicknesses of internal apertures and the TopPlate.

used. The reflectance for $\lambda < 100$ nm is relevant only for incidence angles above 80°, that is, for short wavelengths or high energy photons only grazing incidence is relevant. The maximum reflected power detected in a single sensor is in the order of 1% for $\lambda < 100$ nm and increases up to 2% for $\lambda > 100$ nm. Note that typical machining processes will result in reflection coefficients in line with a roughness parameter of about 0.25 [16]. Additional coatings may improve this value. For ITER, it is foreseen to add an mm-wave absorbing ceramic coating to the inside of bolometer cameras [6] which offers a gray surface that is significantly rougher than any machining process. However, as the reflection coefficient of this coating has not been determined so far, the remainder of this article assumes a roughness parameter of 0.25 as a conservative approach.

Fig. 7 shows the variation of the thickness of internal apertures. In this graph, the maximum power recorded for each geometric configuration and wavelength has been normalized to the maximum power for the given wavelength. The graph shows that with increasing aperture thickness the amount of reflected light will increase, too, irrespective of wavelength. Additionally, a configuration with the thinnest internal aperture of 0.5 mm has been combined with reducing the thickness of the TopPlate from the standard value of 5 to 2 mm showing a further reduction in reflections. Accordingly, the preferred solution for ITER would be to implement internal apertures with 0.5 mm thickness and a TopPlate with 2 mm thickness.

This article has been accepted for inclusion in a future issue of this journal. Content is final as presented, with the exception of pagination.

MEISTER et al.: OPTIMIZING ITER BOLOMETER CAMERAS IN VIEW OF INTERNAL REFLECTIONS
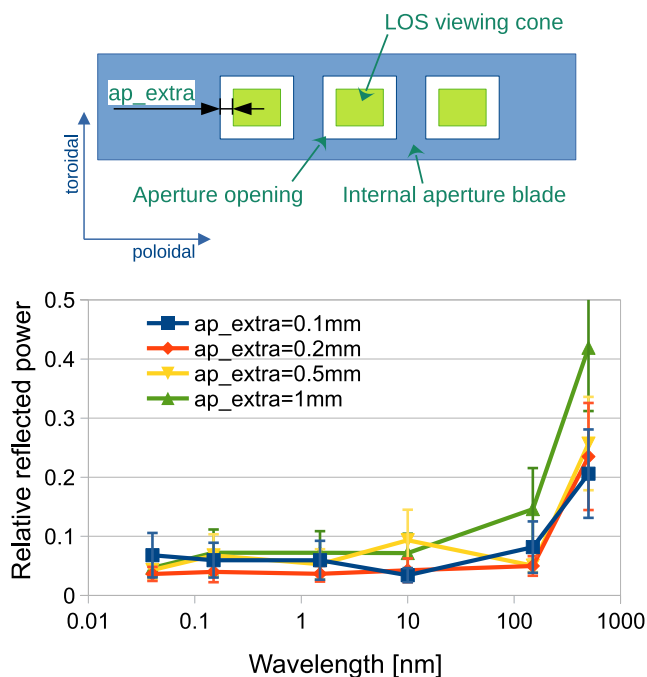5

Fig. 8. Variation of the size of openings for internal apertures with extra space around the viewing cone (top) and impact on relative reflected power (bottom).

Fig. 9. Relative reflected power for a collimator with ten channels and four nonequidistant or five equidistant internal apertures.

Another geometric variation investigated was to assess how much it is possible to increase the size of the openings for internal apertures beyond the dimensions of the viewing cones without increasing the amount of internal reflections. This extra space in both toroidal and poloidal directions around the viewing cone, as sketched on top of Fig. 8 (the purpose of which is to avoid vignetting of the viewing cones by the internal apertures due to manufacturing and assembly tolerances), has been varied between 0.1 and 1 mm. This is to be compared to the poloidal extent of the viewing cone which increases from 1.5 mm at the sensor up to 7.7 mm at the front aperture. As Fig. 8 shows, reflections increase only for an extra space of 1 mm (or higher) and only for $\lambda > 100$ nm. This result is consistent with previous findings. The grazing incident reflections do not vary strongly with only a minor increase in the aperture size as this does not change the angle of incidence significantly. But beyond a certain aperture size, there is more scope for multiple reflected rays reaching the sensors.

Based on the simulation results presented so far in this section, a five-channel collimator with the viewing geometry as given in Section II is optimized if equipped with four equidistant internal apertures of 0.5 mm thickness and extra space for their openings of 0.5 mm.

In ITER port-mounted cameras, typical collimators combine ten channels. A typical geometry producing the desired viewing cones is shown in Fig. 3 on the right. Such a collimator can suppress crosstalk either with five equidistant internal apertures or with four nonequidistant ones. As shown in Fig. 9, these two configurations are equivalent in terms of internal reflections. Due to the fewer number of components, the
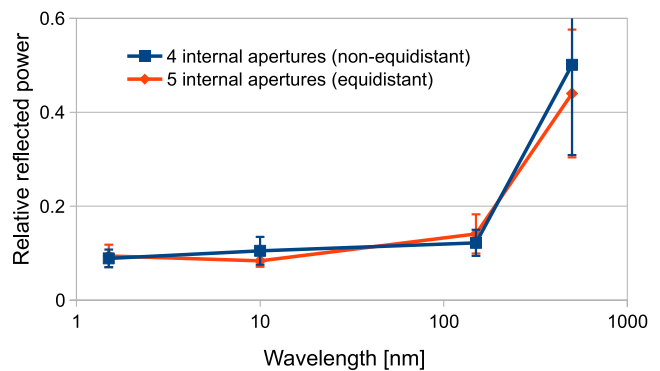
version with four nonequidistant internal apertures would be preferred in terms of manufacturing.

IV. SYNTHETIC DIAGNOSTIC FOR ITER

The results of Sections II and III have been used to establish a synthetic diagnostic setup for assessing the impact of camera internal reflections on expected plasma radiation measurements in ITER.

A. Setup of Synthetic Diagnostics

Collimator geometry and materials have been defined according to the results of Section III-B and implemented for two five-channel collimators in a virtual scene representing ITER using the Python libraries Cherab [19], [20] and Raysect [15]. The resulting geometry for one representative camera in the upper port plug (green) and one in the equatorial port plug (blue) is shown in Fig. 10 (left). This figure also shows a zoom into the diverter region (right) identifying the numbering of individual channels for both cameras. The simulations used the wavelength-resolved radiation profile of a typical impurity-seeded ITER plasma as a light source (see Section IV-B). The simulations have been run to detect the power in each sensor individually for each wavelength bin and sampling 10^4 samples per wavelength bin in case of collimators having been assigned 25% roughened Cu as material (see Section III-A) or 10^6 samples per wavelength bin in the case of considering fully absorbing surfaces. In all cases, the in-vessel components of ITER has been modeled as fully absorbing surfaces, thus ignoring in-vessel reflections.

B. Wavelength-Resolved Radiation Map

As the ray-tracing simulations of camera internal reflections have demonstrated that there is a strong dependence on the wavelength, a wavelength- resolved radiation map has been created to investigate the potential impact on bolometer measurements in ITER. The background plasma used is a typical impurity-seeded ITER plasma with a high radiation fraction ([21], Fig. 7 (case 1)]). Parameters of the background plasma have been taken from the JINTRAC shot 134 000, run 60, for inside the separatrix and from the SOLPS shot 123 303, run 1, for outside the separatrix (scrape-off layer, edge, and

This article has been accepted for inclusion in a future issue of this journal. Content is final as presented, with the exception of pagination.

6   IEEE TRANSACTIONS ON PLASMA SCIENCE
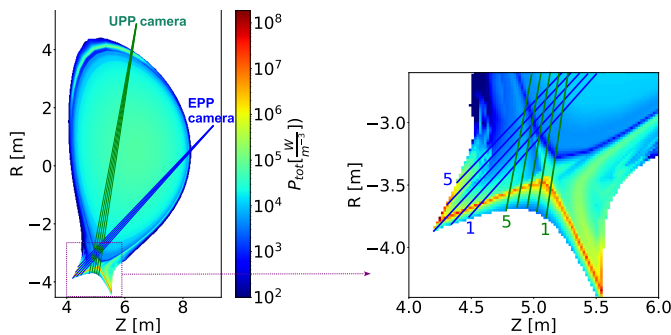

Fig. 10. Viewing geometry used for the simulations of the synthetic diagnostic with the total radiation intensity based on the radiation map from Section IV-B.
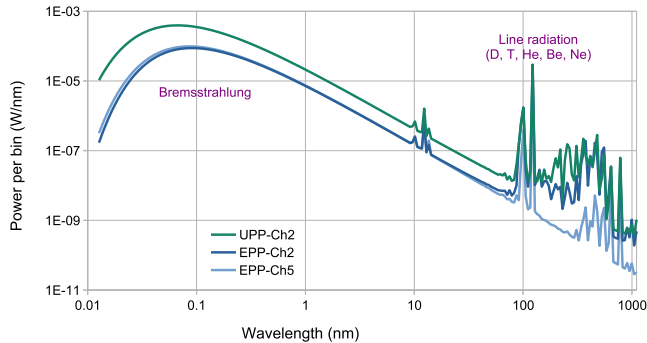

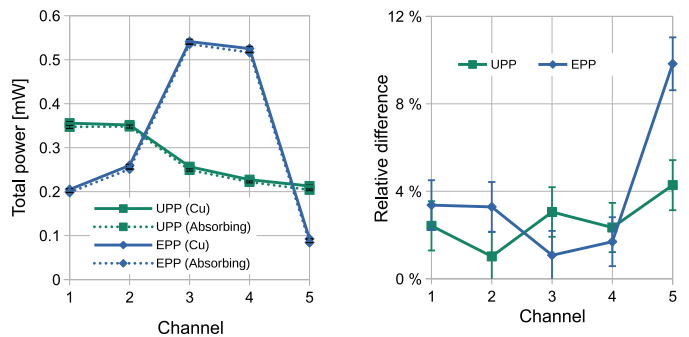Fig. 11. Detected power per wavelength bin for three channels.

Fig. 12. Total power per channel measured by synthetic diagnostic in the case of Cu (continuous lines) or fully absorbing surfaces (dotted lines) as material for collimators (left). Relative difference between the two cases (right).

diverter region). Based on the background plasma the radiation contributions have been calculated for Bremsstrahlung using Cherab internal routines and for line radiation using the photon emissivity coefficients from ADAS (adf15 for D and T, adf208 for Be, He, and Ne) [22]. In total, 238 wavelength bins have been defined evenly in logarithmic scale to cover the wavelength range from 0.012 up to 1240 nm in the case of fully absorbing surfaces and 25 bins of 50 nm width from 0 up to 1250 nm.

So far, the total radiated energy from the underlying simulated plasmas could be reproduced only within a factor of 2. The reason is that contributions from the photorecombination continuum still need to be added to the calculations. Furthermore, contributions from individual species should be verified for completeness.

C. Synthetic Diagnostic Results

The line-integrated power per wavelength bin for three channels with fully absorbing collimator surfaces, that is, suppressing all reflections, is shown exemplarily in Fig. 11. From such simulations, it has been calculated that 91%–98% of the power from the plasma detected in sensors is for $\lambda < 200$ nm, depending on the exact path of the LOS through the plasma.

Fig. 12 (left) shows the total power measured in each channel for the case of using Cu with a roughness parameter of 0.25 as surface material of collimators (continuous lines) and compares it to the case of using fully absorbing surfaces (dotted lines), that is, comparing the case with and without reflections, respectively. The right side of this figure shows the relative difference between the two cases. Within the

simulation uncertainties, there is an enhanced contribution from reflections of about 3% apparent. According to the results of Section III-B, this is a combination of grazing incidence reflections for short wavelengths and multiple reflections for long wavelengths. Channel five of the camera in EPP shows a larger difference. The reason is most likely that this channel observes the lowest signal and the difference between the case with and without reflections is subject to higher uncertainty than the ray-tracing simulations suggest.

V. CONCLUSION

The internal design of collimators for port-mounted bolometer cameras on ITER has been optimized. A procedure has been developed to optimize the number of internal apertures to prevent crosstalk of light. For the case of port-mounted cameras in ITER four equidistant or nonequidistant internal apertures, depending on the geometric parameters of the corresponding viewing cones, have been identified as optimal. Camera internal reflections have been investigated on a representative collimator using the ray-tracing library Raysect. They are most relevant for $\lambda > 100$ nm and contribute up to 2% to the signal. For $\lambda < 100$ nm grazing incidence reflections on internal apertures and TopPlate add about 1% to the signal. Camera internal reflections can be minimized by reducing the thickness of internal apertures to 0.5 mm (a compromise between reflections and structural integrity under ITER loads) and reducing the thickness of the TopPlate to below 5 mm (exact value to be determined in view of required attenuation of mm-waves [6]). Manufacturing and assembly tolerances of the openings of internal apertures may be relaxed by adding a margin of 0.5 mm to the minimum size of their openings. Applying these findings to an optimized collimator geometry, two sample collimators have been implemented as synthetic diagnostics in an ITER environment using the libraries Cherab and Raysect. Generating a dedicated spectrally resolved radiation map based on a simulated impurity-seeded discharge of ITER and using it as a light source, it could be shown that collimator internal reflections increase the total detected power by about 3% or more, depending on the observed spectral distribution of the radiation.

The presented characterization of reflections inside bolometer cameras is the most relevant for wavelengths $\lambda > 100$ nm. It is also a conservative assessment for port-mounted bolometer cameras for ITER due to the

intention to apply a rough mm-wave absorbing coating [6]. Given the many different sources of uncertainty listed in the introduction, the overall tolerable level of uncertainty of 5%, and the contribution of reflections found, it seems necessary to reduce the impact of reflections on the overall uncertainty by accounting for them to first order in the data analysis (such as by including the ray-tracing modeling as presented herein the geometric description) assuming that second-order effects that are not accounted for do not contribute more than 1% to the error (such as the spectral dependence that probably can only be accounted for imperfectly even if consolidated wavelength-resolved radiation profiles are available). Thus, as far as reflections in cameras are concerned, one can anticipate that the ITER requirements seem feasible. However, it is evident that to achieve the measurement requirements, commissioning and data processing on ITER will require a much higher level of attention than is common on present-day fusion experiments and that several effects identified will need to be accounted for accurately in the data analysis, at least to first order.

ACKNOWLEDGMENT

REFERENCES

[1] K. F. Mast, J. C. Vallet, C. Andelfinger, P. Betzler, H. Kraus, and G. Schramm, "A low noise highly integrated bolometer array for absolute measurement of VUV and soft X radiation," *Rev. Sci. Instrum.*, vol. 62, no. 3, pp. 744–750, Mar. 1991.

[2] H. Meister et al., "Bolometer developments in diagnostics for magnetic confinement fusion," *J. Instrum.*, vol. 14, no. 10, p. C10004, Oct. 2019.

[3] L. C. Ingesson, B. Alper, B. J. Peterson, and J.-C. Vallet, "Chapter 7: Tomography diagnostics: Bolometry and soft-x-ray detection," *Fusion Sci. Technol.*, vol. 53, no. 2, pp. 528–576, 2008, doi: 10.13182/FST53-528.

[4] A. J. H. Donné et al., "Chapter 7: Diagnostics," *Nucl. Fusion*, vol. 47, no. 6, p. S337, 2007.

[5] L. C. Ingesson, A. Doblas, A. Gandhi, S. Jahanbakhsh, and H. Meister, "Generic approach to assess the measuring performance of total-radiated power quantities by multi-channel resistive bolometer diagnostics on fusion experiments," *Rev. Scientific Instrum.*, vol. 95, no. 1, Jan. 2024, Art. no. 013505.

[6] H. Meister, W. Kasparek, D. Zhang, M. Hirsch, J. Koll, and A. Zeitler, "Millimetre wave attenuation of prototype diagnostic components for the ITER bolometers," *Fusion Eng. Design*, vols. 96–97, pp. 861–864, Oct. 2015.

[7] H. Meister et al., "Development of an automated method for in situ measurement of the geometrical properties of the ITER bolometer diagnostic," *Fusion Eng. Design*, vol. 86, nos. 6–8, pp. 1170–1173, Oct. 2011.

[8] F. Penzel et al., "Assessment of line of sight characteristics of ITER bolometer prototype collimators," *Fusion Eng. Design*, vol. 88, nos. 6–8, pp. 1267–1270, 2013.

[9] S. Jahanbakhsh et al., "Calibration and thermal test results of prototype bolometer sensors for ITER fusion reactor," *Rev. Scientific Instrum.*, vol. 94, no. 3, Mar. 2023, Art. no. 033503.

[10] H. Meister, S. Jahanbakhsh, D. Zhang, L. C. Ingesson, and A. Pataki, "Effects of neutral gas pressure on calibration parameters of resistive bolometer sensors in fusion devices," submitted for publication.

[11] F. Penzel, H. Meister, L. Giannone, and D. Zhang, "Calibration parameter drift compensation of metal resistive bolometers operating in a thermal varying environment," *Fusion Eng. Design*, vol. 121, p. 100, Oct. 2017.

[12] M.-H. Aumeunier et al., "Infrared thermography in metallic environments of WEST and ASDEX upgrade," *Nucl. Mater. Energy*, vol. 26, Mar. 2021, Art. no. 100879.

[13] H. Meister and S. Kalvin, "Optimisation of design parameters for collimators and pin-holes of bolometer cameras," *Fusion Eng. Design*, vol. 89, no. 12, pp. 3039–3045, Dec. 2014.

[14] K. McCormick et al., "New bolometry cameras for the JET enhanced performance phase," *Fusion Eng. Design*, vol. 74, nos. 1–4, pp. 679–683, Nov. 2005.

[15] A. Meakins and M. Carr. (2021). *Raysect, an Oop Ray-Tracing Framework for Python, V0.8*. [Online]. Available: http://www.raysect.org/index.html

[16] H. Langer, A. Steinbicker, H. Meister, and C. Zauner, "Integrated thermal FE analyses and testing of prototype components for the ITER bolometer diagnostic," *Fusion Eng. Design*, vols. 96–97, pp. 821–825, Oct. 2015.

[17] H.-J. Hagemann, W. Gudat, and C. Kunz, "Optical constants from the far infrared to the X-ray region: Mg, Al, Cu, Ag, Au, Bi, C, and Al_2O_3," *J. Opt. Soc. Amer.*, vol. 65, no. 6, pp. 742–744, Jun. 1975.

[18] H.-J. Hagemann, W. Gudat, and C. Kunz, "Optical constants from the far infrared to the X-ray region: Mg, Al, Cu, Ag, Au, Bi, C, and Al_2O_3," Deutsches Elektron Synchrotron DESY, Hamburg, Germany, Tech. Rep. DESY SR-74/7, 1974. [Online]. Available: https://refractiveindex.info/?shelf=main&book=Cu&page=Hagemann

[19] M. Carr et al., "Towards integrated data analysis of divertor diagnostics with ray-tracing," in *Proc. EPS Conf. Plasma Phys.*, 2017, pp. 1–4. [Online]. Available: http://ocs.ciemat.es/EPS2017PAP/pdf/O5.130.pdf

[20] M. Carr et al., "Description of complex viewing geometries of fusion tomography diagnostics by ray-tracing," *Rev. Scientific Instrum.*, vol. 89, no. 8, Aug. 2018, Art. no. 083506.

[21] J. D. Lore, X. Bonnin, J.-S. Park, R. A. Pitts, and P. C. Stangeby, "High gas throughput SOLPS-ITER simulations extending the ITER database to strong detachment," *Nucl. Fusion*, vol. 62, no. 10, Sep. 2022, Art. no. 106017.

[22] H. P. Summers. (2004). *The ADAS User Manual, Version 2.6*. [Online]. Available: http://www.adas.ac.uk